Computational Fluid Dynamics of Particle Transport and Deposition

Goodarz Ahmadi

Department of Mechanical and Aeronautical Engineering, Clarkson University, Potsdam, NY 13699-5725, USA

1. INTRODUCTION

In many environmental and industrial applications, small particle transport and deposition play a critical role. Particle dispersion and deposition in turbulent

flow field have attracted considerable attention due to their wide applications in xerography, microcontamination control, microelectronic, xerographic, aerospace, and chemical industries, as well as air pollution controls, waste disposal, and many other environmental fields.

Pollutant transport and deposition in indoor air, in urban areas, as well as in the respiratory airways are of particular health interest. New application areas, such as therapeutic drug delivery, are also continuously emerging. Many energy-related industrial processes such as fluidized bed combustor and fuel spray in internal combustion engine involve transport, deposition, and resuspension of small particles. Fuchs [1], Friedlander [2], and Hinds [3] provided extensive reviews of particles' transport processes. Many applications of particle adhesion and detachment were described by Mittal [4] and Quesnel et al. [5], among others.

Here a review of the literature on computational modeling of airflow and particle motion is presented. Friedlander and Johnstone [6] developed a theory for particle deposition in turbulent flows using the concept of "free flight." Additional works in this direction were reported by Fernandez de la Mora and Friedlander [7], among others. Cleaver and Yates [8] suggested an inertial deposition mechanism during the "turbulent burst" as the key deposition mechanism. Progress along this line was reported by Fichman et al. [9], and Fan and Ahmadi [10–14]. Computer simulations of particle deposition in ducts were reported by Li and Ahmadi [15–18], He and Ahmadi [19], and Shams et al. [20], among others.

Li, Ahmadi and co-workers [21], Ahmadi and Smith [22], and He and Ahmadi [19] used anisotropic turbulence models for analyzing particle transport and deposition analysis in complex regions. Direct numerical simulation studies of particle deposition rate in turbulent channel flows were performed by McLaughlin [23], Ounis et al. [24,25], Squires and Eaton [26], Soltani and Ahmadi [27,28], Soltani et al. [29], and Zhang and Ahmadi [30]. The effect of lift on particle deposition was studied by Wang et al. [31]. A review of earlier works on direct numerical simulation was provided by McLaughlin [32].

Applications of particle transport and deposition to microcontamination control were described by Cooper et al. [33,34] and more recently discussed by Rader and Geller [35], Lin and Zhu [36], and Liu [37].

In this chapter, fundamentals of computational modeling of particles transport and deposition in turbulent flows are described. Particular attention is given to proper modeling of the fluctuation field of airflow turbulence. The Lagrangian particle trajectory analysis procedure is outlined. The hydrodynamic forces including drag and lift acting on small particles suspended in air are discussed, and the importance of Cunningham slip correction as well as the Brownian motion for nano-size particles is pointed out. Sample applications of computational modeling of aerosol transport and deposition in human airway passages are presented.

2. FORMULATION

2.1. Fundamentals of Computational Fluid Dynamics

In this section, computational fluid dynamics for simulating laminar and turbulent flows is described. It is well known that many fluids and certainly airflows are governed by the celebrated Navier–Stokes and the continuity equations. For an incompressible flow, these are given as:

$$\nabla \cdot \mathbf{u} = 0, \tag{1}$$

and

$$\rho \frac{d\mathbf{u}}{dt} = -\nabla p + \mu \nabla^2 \mathbf{u} + \rho \mathbf{f} \tag{2}$$

where ρ is the constant density of fluid, $\mathbf{u}$ is velocity vector, p is the pressure, μ is the coefficient of viscosity, and $\mathbf{f}$ is the body force per unit mass. Equations (1) and (2) form four equations for evaluating the velocity and the pressure field under the "laminar" flow condition. The applicability of the Navier–Stokes equations for predicting the behavior of laminar flows has been well established [38,39].

When the velocity increases, and the so-called "Reynolds number" crosses a certain limit, the laminar airflow pattern goes through a transient and becomes turbulent. In turbulent flows, the field properties become random functions of space and time. Decomposing the velocity and pressure into mean and fluctuation values and averaging the Navier–Stokes equation leads to the Reynolds equation. That is,

$$\frac{\partial U_i}{\partial t} + U_j \frac{\partial U_i}{\partial x_j} = -\frac{1}{\rho} \frac{\partial P}{\partial x_i} + \nu \frac{\partial^2 U_i}{\partial x_j x_j} - \frac{\partial \overline{u_i' u_j'}}{\partial x_j} \tag{3}$$

where U_i and P are mean velocity and mean pressure and u_i' is the fluctuation component of velocity. The last term in Eqn (3) is related to the so-called Reynolds stress (turbulent stress):

$$\tau_{ij}^T = -\rho \overline{u_i' u_j'} \tag{4}$$

The Reynolds stress produces six new unknowns that need to be evaluated into the momentum equation. Many phenomenological models such as Prandtl mixing length theory were developed in early 1900 to relate the Reynolds stress to the mean flow properties [39,40]. With the availability of high-power computers and advanced computational techniques, a number of more detailed multi-equation turbulence models have been developed. One model that has used extensively and now has been implemented into most commercial codes is the k–ε model [41,42]. Accordingly, it is assumed that Reynolds stresses are linearly related to the mean deformation field similar to a Newtonian fluid. That is,

$$-\overline{u_i' u_j'} = \nu_T \left(\frac{\partial U_i}{\partial x_j} + \frac{\partial U_j}{\partial x_i} \right) - \frac{2}{3} k \delta_{ij} \tag{5}$$

where

$$\nu_T = \frac{c_\mu k^2}{\varepsilon} \tag{6}$$

is the eddy (turbulent) viscosity, which is related to the kinetic energy of turbulence fluctuation, k, and turbulence dissipation rate, ε. The corresponding closed transport equations are k and ε given by

$$\frac{\partial k}{\partial t} + U_j \frac{\partial k}{\partial x_j} = \frac{\partial}{\partial x_j} \left(\frac{\nu_T}{\sigma_k} \frac{\partial k}{\partial x_j} \right) + \nu_T \left(\frac{\partial U_i}{\partial x_j} + \frac{\partial U_j}{\partial x_i} \right) \frac{\partial U_i}{\partial x_j} - \varepsilon \tag{7}$$

$$\frac{\partial \varepsilon}{\partial t} + U_j \frac{\partial \varepsilon}{\partial x_j} = \frac{\partial}{\partial x_j} \left(\frac{\nu_T}{\sigma_\varepsilon} \frac{\partial \varepsilon}{\partial x_j} \right) + c_{\varepsilon 1} \nu_T \frac{\varepsilon}{k} \left(\frac{\partial U_i}{\partial x_j} + \frac{\partial U_j}{\partial x_i} \right) \frac{\partial U_i}{\partial x_j} - c_{\varepsilon 2} \frac{\varepsilon^2}{k} \tag{8}$$

where the terms on the right-hand side of Eqns (7) and (8) correspond, respectively, to diffusion, production, and dissipation. The generally accepted values of the constants are [42]:

$$c_\mu = 0.09, \quad c_{\varepsilon 1} = 1.45, \quad c_{\varepsilon 2} = 1.9, \quad \sigma_k = 1, \quad \sigma_\varepsilon = 1.3 \tag{9}$$

while the k–ε model has been used extensively in industrial applications, it has several limitations. One important limitation is that it is an isotropic model and cannot account for the anisotropy of turbulent normal stresses.

To overcome the limitation of the isotropic turbulence models, Reynolds stress transport models (RSTMs) have been developed. In this approach, transport equations for the evaluation of the components of the Reynolds stresses are developed and closed. An earlier model of this kind was developed by Launder, Reece, and Rodi [43]. The corresponding closed Reynolds stress transport model (RSTM) that is used in some of the commercial codes is given as

$$\left(\frac{\partial}{\partial t} + U_k \frac{\partial}{\partial x_k} \right) \overline{u_i' u_j'} = - \left[\overline{u_i' u_k'} \frac{\partial U_j}{\partial x_k} + \overline{u_j' u_k'} \frac{\partial U_i}{\partial x_k} \right]$$
$$- \frac{2}{3} \delta_{ij} \varepsilon - c_1 \frac{\varepsilon}{k} \left(\overline{u_i' u_j'} - \frac{2}{3} \delta_{ij} k \right) + \left(\varphi_{ij}^{(2)} + \varphi_{ji}^{(2)} \right)$$
$$+ c_s \frac{\partial}{\partial x_k} \left[\frac{k}{\varepsilon} \left(\overline{u_i' u_l'} \frac{\partial}{\partial x_l} \overline{u_j' u_k'} + \overline{u_j' u_l'} \frac{\partial}{\partial x_l} \overline{u_k' u_i'} + \overline{u_k' u_l'} \frac{\partial}{\partial x_l} \overline{u_i' u_j'} \right) \right] \tag{10}$$

where $\varphi_{ij}^{(2)} + \varphi_{ji}^{(2)}$ is collectively called the "Rapid Term" and in its simplest form is given as

$$\varphi_{ij}^{(2)} + \varphi_{ji}^{(2)} = -\gamma \left(P_{ij} - \frac{2}{3} P \delta_{ij} \right) \tag{11}$$

in Eqn (11), P_{ij} is the turbulence energy production with $P = P_{ii}$, δ_{ij} is the Kronecker delta, and c_1, c_s, and γ are constant parameters. When the RSTM is used, there is still the need to use a transport equation for the turbulence dissipation rate, ϵ, such as the one given by Eqn (8).

2.2. Diffusion Model

The Eulerian diffusion approach is used for gaseous pollutants, which are treated as transferable scalars. The corresponding convection–diffusion equation for species transport is given as

$$\frac{\partial C^\alpha}{\partial t} + u_j \frac{\partial C^\alpha}{\partial x_j} = \frac{\partial}{\partial x_j}\left(\left(D^\alpha + \frac{\nu_t}{Sc_t^\alpha}\right)\frac{\partial C^\alpha}{\partial x_j}\right) \tag{12}$$

where C^α is the concentration of pollutant species α and D^α is its diffusivity, ν_t is the turbulence eddy viscosity, and $Sc_t^\alpha = \nu_t/D_t^\alpha$ is turbulence Schmidt number, with D_t^α being the turbulent diffusivity of species α.

Equation (12) is also applicable to ultrafine (nano) particulate materials. The particle diffusivity then is given as

$$D^\alpha = \frac{k_\beta T C_c}{3\pi\mu d} \tag{13}$$

where, d is the diameter of the particle, $k_b = 1.38 \times 10^{-23}$ J/K is the Boltzmann constant, and T is the temperature. For large particles, the inertial effects become important and the validity of Eqn (12) becomes questionable. Also, when an external force acts on the particles, the diffusion equation could be modified and rewritten as

$$\frac{\partial C^\alpha}{\partial t} + \left(u_j + u_j^T\right)\frac{\partial C^\alpha}{\partial x_j} = \frac{\partial}{\partial x_j}\left(\left(D^\alpha + \frac{\nu_t}{Sc_t^\alpha}\right)\frac{\partial C^\alpha}{\partial x_j}\right) \tag{14}$$

where u_j^T is the terminal velocity of the particles subject to the external forces field. Equation (14) accounts for the steady response of particle to the external force field, but it is an approximation in that it does not include the transient response of the particles that depends on their inertia.

2.3. Particle Equation of Motion

The Lagrangian simulation procedure for particle transport is described in this section. The range of diameters of particles considered is between a few nanometers and about 30 μm. The lower limit roughly corresponds to the transition from molecule to particle. Particles larger than 30 μm normally do not remain suspended in air for a sufficient amount of time.

The Lagrangian equation of motion of a particle suspended in a fluid is given as

$$\frac{du_i{}^p}{dt} = \frac{1}{\tau}\frac{C_D Re_p}{24}\left(u_i - u_i{}^p\right) + F_i^L + g_i + n_i(t) \tag{15}$$

where $u_i^p = dx_i/dt$ is the particle velocity, F_i^L is the lift force, g_i is acceleration of gravity, $n_i(t)$ is the Brownian force per unit mass, and τ is the particle relaxation time given as

$$\tau = \frac{d^2 \rho^p C_c}{18\mu} = \frac{Sd^2 C_c}{18\nu}, \tag{16}$$

where ρ^p is the particle density, ν is the coefficient of kinetic viscosity, $S = \rho^p/\rho$ is the density ratio, and C_c is the Cunningham correction factor.

In Eqn (15), C_D is the drag coefficient given as

$$C_D = \frac{24}{Re_p}(1 + 0.15Re_p^{0.687}) \quad \text{for } Re_p < 400 \tag{17}$$

where Re_p is the particle Reynolds number defined as

$$Re_p = \frac{d\left|u_j - u_j^p\right|}{\nu} \tag{18}$$

The lifting force in Eqn (15) is given as

$$F_i^L = \frac{2K\nu^{1/2}d_{ij}}{Sd(d_{lk}\, d_{kl})^{1/4}}\left(u_j - u_j^p\right) \tag{19}$$

where $K = 2.594$ is the constant coefficient of Saffman lift force and d_{ij} is the deformation rate tensor given by

$$d_{ij} = \frac{1}{2}\left(\frac{\partial u_i}{\partial x_j} + \frac{\partial u_j}{\partial x_i}\right) \tag{20}$$

Note that the Saffman lift force is subject to certain Reynolds number limitations:

$$Re_p = \frac{|u - u^p|d}{\nu} \ll 1, \; Re_G = \frac{\dot{\gamma}d^2}{\nu} \ll 1, \; \varepsilon = \frac{Re_G^{1/2}}{Re_p} \gg 1, \tag{21}$$

The Brownian excitation, $n_i(t)$, is modeled as a Gaussian white-noise random process with a spectral density S_0, given as [15]

$$S_0 = \frac{216\nu k_b T}{\pi^2 \rho d^5 S^2 C_c} \tag{22}$$

where $k_b = 1.38 \times 10^{-23}$ J/K is the Boltzmann constant and T is the absolute temperature.

The Cunningham correction factor, which becomes very important for nanoparticles, is given as

$$C_c = 1 + \frac{2\lambda}{d}\left[1.257 + 0.4e^{-1.1d/2\lambda}\right] \tag{23}$$

where λ denotes the molecular mean free path in the gas. Note that $C_c \geq 1$ for all values of d and λ. Further, C_c is about 1 for $Kn = 2\lambda/d < 0.1$ and increases sharply as Kn increases beyond 0.5.

2.4. Turbulence Fluctuations

Equation (15) for particle trajectory analysis includes the effect of hydrodynamic drag force introduced by relative slip velocity, the Saffman lift force due to shear in the flow field, Brownian excitation due to molecular impact, and the gravitational force. The effect of turbulence on transport and dispersion of particles is introduced through the instantaneous fluid velocity, $u_i = U_i + u_i'$. In the turbulent flow field, turbulence diffusion by instantaneous flow fluctuations is the dominant mechanism for particle dispersion and depositions. Therefore, it is critical to incorporate an appropriate model for simulating turbulence fluctuations for accurate analysis of particle transport and deposition processes.

The most accurate procedure for simulation of fluctuation velocity is the direct numerical simulation (DNS). The DNS, however, is currently only practical for low Reynolds number duct flows. The use of large eddy simulation (LES) has also attracted considerable attention. In this approach, large eddies are simulated and the effect of scales smaller than grid size are modeled. While LES can be used for higher Reynolds number flows, the need for computational effort is quite extensive. Also, a completely satisfactory approach for including the subgrid-scale fluctuations on particle dispersion is yet to be developed. For most practical applications, however, turbulence fluctuation is mainly estimated using a variety of stochastic approaches. To account for near wall-coherent eddies, Fan and Ahmadi [10] proposed a sublayer model using a plane stagnation point flow. For reproduction of fluctuation with the stochastic method, Kvasnak et al. [44] employed a probability density function (PDF)-based Langevin equation to generate the instantaneous velocity and velocity gradient fields.

Two commonly used stochastic simulation methods that generate appropriate random field with correct mean-square fluctuation velocities and integral time scales are described in this section.

2.4.1. Continuous Filtered White-Noise (CFWN) Model

The continuous filtered white-noise (CFWN) model was suggested by Thomson [45] for numerical simulation of turbulent fluctuations and is used extensively in the literature and commercial codes [19,46]. In this model, the instantaneous fluid velocity is simulated using the turbulence local mean velocity and mean-square fluctuations via the following Langevin equation:

$$\frac{\mathrm{d}u_i}{\mathrm{d}t} = -\frac{u_i - U_i}{T_{\mathrm{L}}} + \left(\frac{2\overline{u_i'^2}}{T_{\mathrm{L}}}\right)^{1/2} \xi_i(t) \tag{24}$$

where T_L is the Lagrangian integral time scale and $\xi_i(t)$ is a vector Gaussian white-noise random process with spectral density $1/\pi$. The Lagrangian integral time scale T_L in Eqn (24) is estimated using

$$T_L = C_1 \frac{k}{\varepsilon} \tag{25}$$

where C_1 is a constant. The solution of Eqn (24) provides the fluctuation velocity vector at every time step.

2.4.2. Eddy Lifetime Model

The "Eddy Lifetime" model assumes that the particles encounter discrete turbulence eddies. In this model, fluctuation velocity is given as:

$$u_i' = G\sqrt{\overline{u_i'^2}} \tag{26}$$

where G is a zero mean, unit variance normally distributed random number, $\sqrt{\overline{u_i'^2}}$ is the root mean-square (RMS) local fluctuation velocity in the ith direction. The time scale τ_e associated with each eddy (eddy lifetime) is given as

$$\tau_e = 2T_L, \tag{27}$$

where T_L is given by Eqn (25). In addition to the eddy lifetime, a particle eddy crossing time t_{cross} is defined as

$$t_{\text{cross}} = -\tau \ln\left[1 - \left(\frac{L_e}{\tau|u - u^p|}\right)\right] \tag{28}$$

here, τ is the particle relaxation time defined in Eqn (16), L_e is the eddy length scale, and $|u_i - u_i^p|$ is the magnitude of the relative slip velocity. The frequency of the particle encountering turbulence eddies is the reciprocal of the lesser of τ_e and t_{cross}. Therefore, Eqn (26) is used to generate a new random fluctuation velocity when the minimum of the eddy lifetime or eddy crossing is reached.

2.4.3. Near-Wall Quadratic Variation Correction

Conservation of mass requires the root mean-square turbulence fluctuation normal to wall to follow a quadratic variation [15,40]. That is,

$$v^{+\prime} = Ay^{+2} \text{ for } y^+ < 4, \tag{29}$$

where the wall units are used with $y^+ = yu^*/\nu$ and $v^{+\prime} = \sqrt{\overline{v'^2}}/u^*$. Here, the shear velocity is defined as $u^* = \sqrt{\tau_w/\rho}$ and τ_w is the wall shear stress. Using the direct numerical simulation (DNS) of near wall flows, Ounis et al. [25] suggested that $A = 0.008$. Li and Ahmadi [15–17], He and Ahmadi [19], and Tian and Ahmadi [46] included the quadratic variation of the normal fluctuation

velocity in their simulations of particle depositions in turbulent flows and noted its profound effects.

3. APPLICATIONS

Sample applications of the computational modeling approach are described in this section.

3.1. Duct Flows

The computational procedure described earlier was used by He and Ahmadi [19] to simulate particle transport and deposition in a duct flow. Sample model predictions are reproduced in Figs. 2.1 and 2.2, which show the deposition velocity versus particle relaxation time in wall units. Particle diameter is also shown in the figure for clarity. Figure 2.1 shows that the particle deposition velocity follows a v-shaped curve. The deposition velocity is quite high for very small particles due to the increase in the particle diffusivity (Brownian motion). The deposition velocity then decreases as particle size increases, since the particle diffusivity, as given by Eqn (13), decreases with particle diameter. The minimum particle deposition occurs for nondimensional relaxation time of the
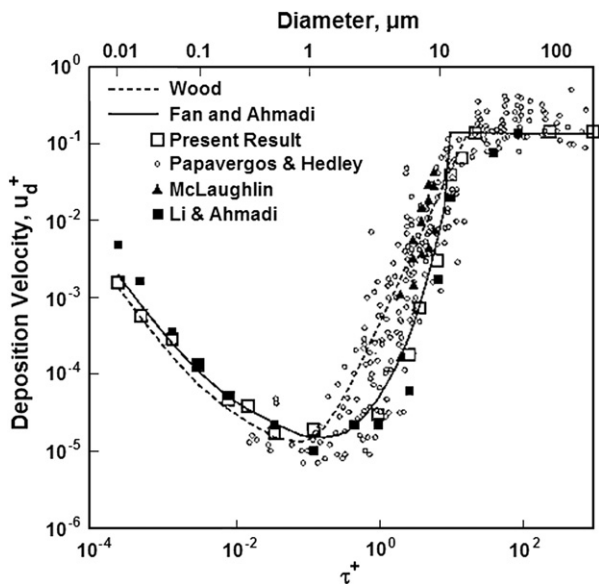

FIGURE 2.1 Comparison of computer simulations of He and Ahmadi [19] for deposition of spherical particles in duct flows with experimental data collected by Papavergos and Hedley [49] and earlier simulation as well as model predictions of Fan and Ahmadi [10,11] and Wood [47,48].
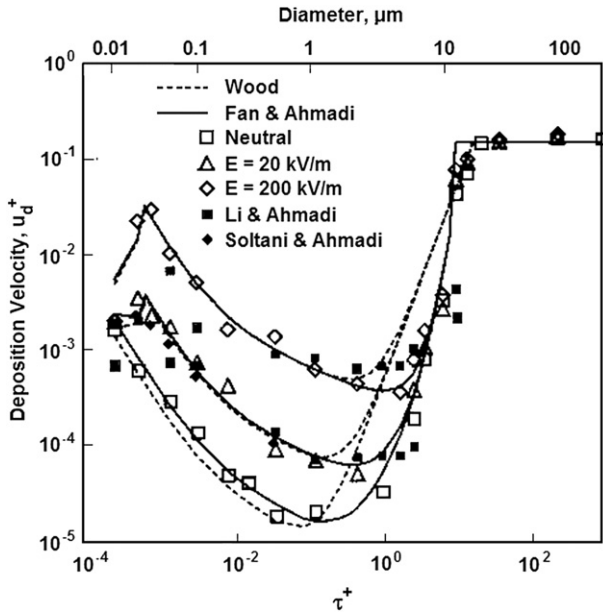
FIGURE 2.2 Comparison of computer simulations of He and Ahmadi [19] and Soltani and Ahmadi [50] for deposition of charged particles in duct flows with the empirical model predictions of Fan and Ahmadi [10,11] and Wood [47,48].

order of 0.1–1 (0.5 μm < d < 5 μm). The deposition velocity then increases for larger relaxation time despite the decrease in the particle diffusivity. This is due to the interaction of these relatively large particles with turbulent eddies [47,48]. The inertia of these relatively large particles affects their transport in turbulent eddies, and their deposition rate increases. For particles with nondimensional relaxation time larger than 15–20, deposition velocity approaches a saturation level of about 0.14. This is because of the very large inertia of the particles in this size range. Figure 2.1 shows good agreement of simulation results of He and Ahmadi [19] with the experimental data collected by Papavergos and Hedley [49], the earlier computer simulations of Li and Ahmadi [16–17] and McLaughlin [23], and the semi-empirical model predictions.

Wood [47,48] has suggested a simple empirical equation for the nondimensional deposition velocity. Accordingly,

$$u_d^+ = 0.057 S_c^{-2/3} + 4.5 \times 10^{-4} \tau^{+2}, \tag{30}$$

where $S_c = v/D$ is the Schmidt number. Fan and Ahmadi [10] developed an empirical equation for deposition of particles in vertical ducts including the effects of surface roughness and gravity along the flow direction, which is given as

$$u_d^+ = \begin{cases} 0.084 S_c^{-2/3} + \dfrac{1}{2}\left[\dfrac{\left(0.64k_r^+ + \frac{1}{2}d^+\right)^2 + \dfrac{\tau^{+2}g^+L_1^+}{0.01085(1+\tau^{+2}L_1^+)}}{3.42 + \left(\tau^{+2}g^+L_1^+\right)/\left(0.01085(1+\tau^{+2}L_1^+)\right)}\right]^{1/\left(1+\tau^{+2}L_1^+\right)} \\[20pt] \qquad \times\left[1 + 8e^{-(\tau^+ - 10)^2/32}\right]\dfrac{0.037}{1 - \tau^{+2}L_1^+(1+(g^+/0.037))} \quad \text{if } u_d^+ < 0.14 \\[12pt] 0.14 \ \ \text{otherwise} \end{cases}$$

(31)

here, $L_1^+ = 3.08/(Sd^+)$, $g^+ = (\nu/u^{*3})g$, and k_r^+ is the surface roughness (zero for smooth surfaces).

Transport and deposition of a charged particle in a duct in the presence of electrostatic forces was studied by He and Ahmadi [19] using the RANS simulation approached described in the earlier sections. Earlier, Soltani et al. [27] and Soltani and Ahmadi [50] simulated charged-particle deposition in a turbulent channel flow using the DNS approach. Their sample model predictions for deposition velocity versus particle relaxation time in wall units are reproduced in Fig. 2.2 for different electric field intensities *E*. Here, it is assumed that the particles carry the Boltzmann charge distribution, which is the natural charge distribution for aerosols in a neutral atmosphere. Figure 2.2 shows that the v-shaped curve for the particle deposition velocity is distorted by the presence of electric field for charged particles smaller than 1 μm. Notably, the deposition velocity peaks for 20 nm particles. This is because the electric force per unit mass reaches its maximum value for 20 nm particles for the Boltzmann charge distribution. For particles larger than a few μm, the effect of electric force on their deposition velocity is relatively small.

3.2. Particle Transport and Deposition in Respiratory Tracts

Particle deposition in the nasal and lung airways has been a subject of great interest due to the health risk of particulate matter (PM) pollutants. Recently, there has been additional interest for the subject by pharmaceutical companies in connection with targeted inhalation therapeutic drug delivery. PM deposition in nose and lung occurs by several mechanisms. Large particles deposit due to impaction, interception, turbulence eddy impaction, and gravitational sedimentation. Particles in the nanometer size range, however, deposit due to turbulence dispersion and Brownian motion.

Effects of airflow and turbulence on particle deposition in the lung were examined by Chan and Schreck [51] using the airflow measurements in hollow casts and airway bifurcation models. Heyder et al. [52] measured total and regional aerosol depositions through the mouth and the nose. Experimental studies for inspiratory particle depositions in a single and double bifurcation

airway were reported by Johnston and Schroter [53], Kim and Iglesias [54], Kim et al. [55], and Kim and Fisher [56].

Deposition of ultrafine particles in replicate cast models of the human nasal cavity was measured by Cohen et al. [57] and Swift et al. [58], among others. Cohen and Asgharian [59] used experimental data and obtained an empirical expression for the deposition efficiency of ultrafine particles by the diffusion mechanism. Recently, Asgharian et al. [60] described a realistic model for lung deposition.

The fluid dynamics of the human larynx and upper tracheobronchial airways was studied by Martonen et al. [61,62]. Balashazy and Hofmann [63,64] and Balashazy [65] analyzed the particle trajectories in a three-dimensional bronchial airway bifurcation. Asgharian and Anjilvel [66] studied the inertial and gravitational depositions in a square cross-section bifurcating passage. Li and Ahmadi [67] studied the particle transport and deposition in first lung bifurcation and included the turbulence dispersion effects. Geometric factors for the quantification of particle deposition patterns in bifurcation airways were studied by Balashazy et al. [68] and Comer et al. [69]. Airflow particle deposition in triple-lung bifurcation was studied by Zhang et al. [70,71] and Zhang and Kleinstreuer [72,73]. Tian et al. [74] recently studied the airflow and deposition pattern in symmetric and asymmetric lung bifurcation models.

Despite a number of studies on particle deposition in human lung, the Brownian diffusion and turbulent dispersion effects were, generally, ignored in the earlier computational models. Martonen et al. [61] pointed out that the flow disturbances from the laryngeal jet could propagate into the trachea and main bronchus. In this section, computational modeling of inspiratory particle transport, dispersion, and deposition in the human nose and lung is described and sample simulation results are presented and discussed. Attention was given to the effects of particle size on the deposition rates and comparison with the available experimental data.

3.2.1. Multi-Bifurcation Airways

Weibel [75] and Raabe et al. [76] have shown that the structure of human bronchial airways can be approximated as a network of repeatedly bifurcating tubes. The bifurcations are generally asymmetric. In most computer models, however, symmetric conditions are assumed.

Recently, Tian et al. [74] have performed a series of computer simulations and compared the particle deposition for symmetric and asymmetric cases. Figure 2.3 shows the sample mesh used in the computations and sample velocity vector field. The mean velocity contours in a plane across the trachea and the left and right bronchus of an adult person are shown in Fig. 2.4. Two different flow rates were considered in these analyses. For a 15-l/min breathing rate, the flow was nearly laminar. For a 60-l/min breathing rate, however, the flow was in a turbulent state of motion. For the turbulence case, the stress transport model was used for the flow analysis and the instantaneous turbulence fluctuations
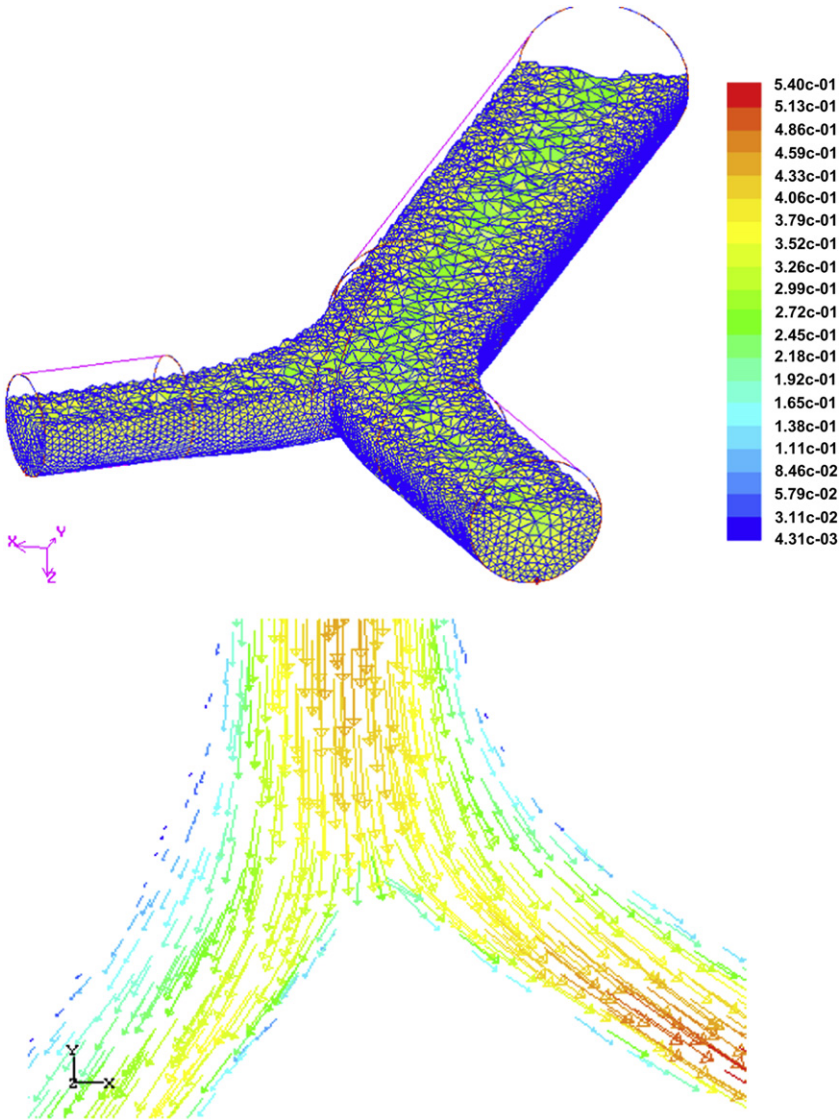
FIGURE 2.3 A sample mesh that was used in the computation and a sample velocity vector field near carina.

were evaluated and were included in the particle trajectory analysis. Figure 2.4 shows that the asymmetric bifurcation leads to regions with higher velocities.

In order to analyze the particle capture efficiency of the upper lung, particles of different diameters were initially released with a uniform distribution at the trachea inlet and their trajectories were analyzed. Figure 2.5 shows the locations

FIGURE 2.4 Mean velocity contours across the upper airways.

of the captured particles of different sizes. It is seen that the relatively large 30-μm particles are mainly deposited on the carina by impaction mechanisms. On the other hand, the 10 nm particles have a more uniform distribution pattern. These small particles are deposited mainly by the diffusion process on the entire passage surface. Very few 1 μm particles are captured by the first lung bifurcation, since for this size range the diffusion is negligible and the inertia is small. These trends of behavior were also observed by Li and Ahmadi [67], among others.

Variations of capture efficiencies of the symmetric and asymmetric first lung bifurcation, as predicted by Li and Ahmadi [67], are compared with the earlier simulations and experimental data for the symmetric case in Fig. 2.6. It is seen that the model predictions are comparable to the experimental data. This figure also shows that the capture efficiency increases sharply as particle Stokes
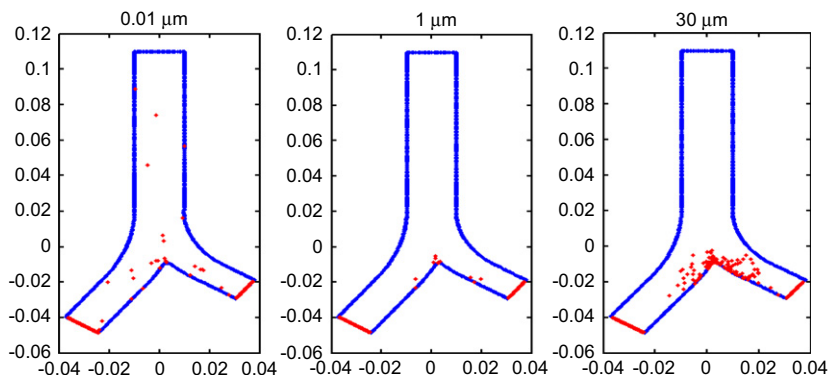

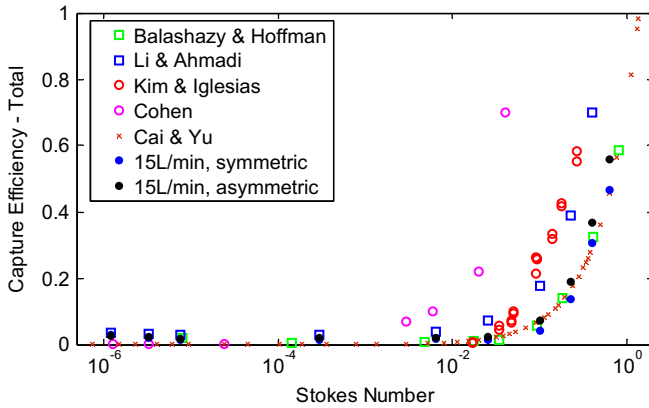**FIGURE 2.5** Deposition pattern for different size particles.

FIGURE 2.6 Comparison of the capture efficiencies versus Stokes numbers.

number increases beyond 0.05. Furthermore, the total capture efficiencies of the symmetric and asymmetric bifurcations do not differ to a noticeable extent.

3.3. Nasal Passages

Early measurements of airflow measurement in the nasal passages were reported by Swift and Proctor [77]. They used a miniature Pitot tube in a nasal cast of a cadaver. Airflow measurements in the nose using hot-wire and hot-film anemometers were reported by Schreck et al. [78] and Hahn et al. [79]. They found that the airflow in the nose was laminar up to a breathing rate of 24 L/min. More recently, Kelly et al. [80] used particle image velocimetry (PIV) on a model fabricated from computed tomography (CT) scans of the nasal passage for their airflow measurements. The common finding of the earlier experimental studies was that the flow regime inside the human nasal cavity for low to moderate breathing rates was laminar. In addition, a large portion of inspired airflow passes through the middle and inferior airways, while a smaller fraction passes through olfactory and meatuses regions.

Computer simulations of airflow inside the human nasal passages were reported by Keyhani et al. [81] and Subramanian et al. [82], among others. They constructed their computational model from magnetic resonance imaging (MRI) of a human subject and used the commercial software FIDAP™ in their analysis. They also showed that a large part of the airflow passed through the middle and inferior airways.

Experimental study of deposition of particles in the human nasal passage was reported by Cheng et al. [83,84], Swift et al. [58,85], and Strong and Swift [86]. Cheng et al. [87], Cheng [88], and Martonen et al. [89] suggested an empirical equation for the capture efficiency of the human nasal passage. Recently, Kelly et al. [90] measured the deposition of ultrafine particles in nasal airway replicas produced by a stereo-lithography machine.

Computer simulation studies of transport and deposition of ultrafine particles in human nasal cavities were reported by Yu et al. [91] and Scherer et al. [92]. In these simulations, a diffusion model for particle deposition was used. Recently, Zamankhan et al. [93] and Shanley et al. [94] presented a series of simulations for particle deposition in the nasal passage of a human male using the Lagrangian particle tracking approach.

Schematics of the cross-section and the geometry of the nasal passage are shown in Figs. 2.7 and 2.8. The sections shown in Fig. 2.7 are obtained from MRI images of an anonymous male donor. These sections were used to construct the computational domain shown in Fig. 2.8. Various regions of the nasal passage are also identified in this figure.

Figure 2.9 shows the unstructured computational mesh that was produced by Zamankhan et al. [93], which included 965,000 tetrahedral elements and 250,000 computational points. A finer computational mesh was also used when needed in those simulations.

The simulated velocity magnitude contours are plotted in Fig. 2.10. Detailed examination of the results shows that more than 70% of the flow passes through the inferior airway, the middle airway, and the region in between on the septum side of the section. About 7% of the flow passes through the olfactory slit, 13% across the three meatus areas, and around 10% across the superior airway. It is seen that the pressure decreases from the nostril to along the nose toward the nasopharynx region. Additional simulation results may be found in the work of Zamankhan et al. [93].

Zamankhan et al. [93] have suggested an empirical expression for the nose friction factor. That is,

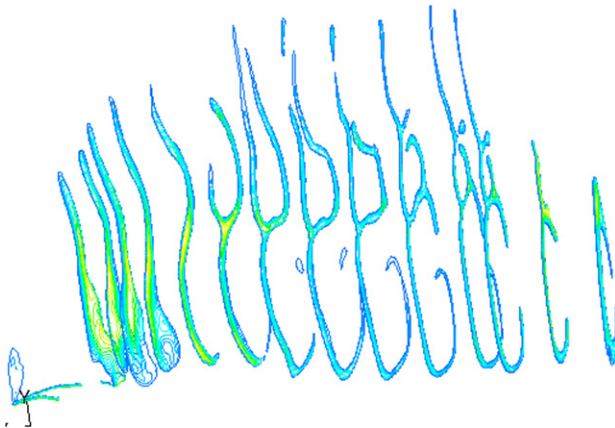$$f = \frac{47.78}{Re}(1 + 0.127Re^{0.489}) \tag{32}$$

FIGURE 2.7 Cross-sections of the nose of a human male obtained from MRI and used in developing the computational model. The contours are velocity magnitudes.
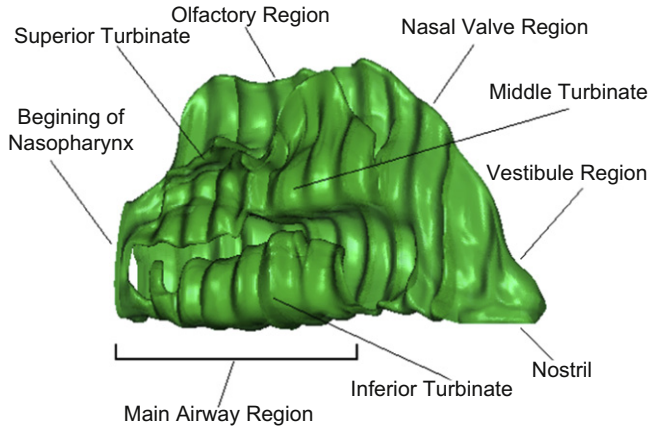
Olfactory Region
Superior Turbinate
Nasal Valve Region
Middle Turbinate
Begining of
Nasopharynx
Vestibule Region
Nostril
Inferior Turbinate
Main Airway Region

FIGURE 2.8 The computational model of the nasal airway with various nose regions.

where the Reynolds number is defined as

$$Re = \frac{u_m d_h}{\nu} \tag{33}$$

where d_h is the average hydrodynamic diameter of the nose coronal sections and u_m is the average flow velocity at the nostril. When the friction factor is
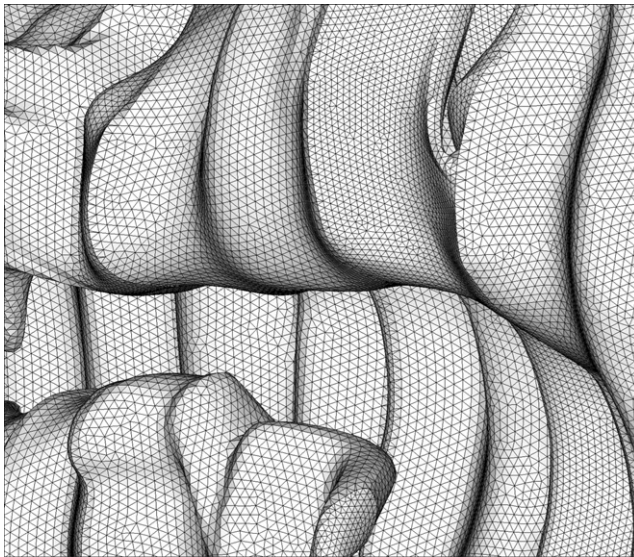

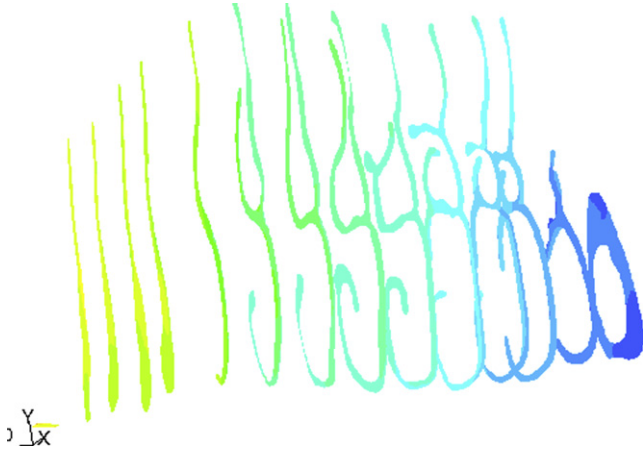**FIGURE 2.9** Sample surface mesh used in the simulations [93].

FIGURE 2.10 Sample velocity vector field in different section of the nasal airways.

given by Eqn (32), the mean pressure drop between the nostril and naso-pharynx, Δp, is given by

$$\frac{\Delta p}{\rho} = f\frac{L}{d_h}\frac{u_m^2}{2}$$

(34)

where L is the passage length and ρ is the air density.

To study particle transport and deposition in the nasal passage, particles of different sizes were introduced at the nostril with a uniform distribution, and their corresponding trajectories were analyzed. For a breathing rate of 4 L/min, the capture efficiency of the nose for different size particles smaller than 100 nm was evaluated and compared with the experimental data of Swift et al. [58] and Cheng et al. [95], as shown in Fig. 2.11. Here, the solid lines correspond to the model prediction. While there are some scatters in the experimental data, this figure shows that the predicted capture efficiencies are in good agreement with the experimental data, particularly for particles smaller than 20 nm. The model prediction for particles larger than 20 nm is, however, somewhat higher than the average of the experimental data.

Zamankhan et al. [93] discussed the potential reason for the discrepancy and also performed a series of simulations with more refined mesh. Accordingly, while the discrepancy can be reduced by using a finer mesh, some deviations remain due to the computational errors introduced by the linear interpolation used.

Figure 2.12 shows the simulated capture efficiencies results for particles smaller than 100 nm versus (inverse) Peclet number. Here Peclet number is defined as

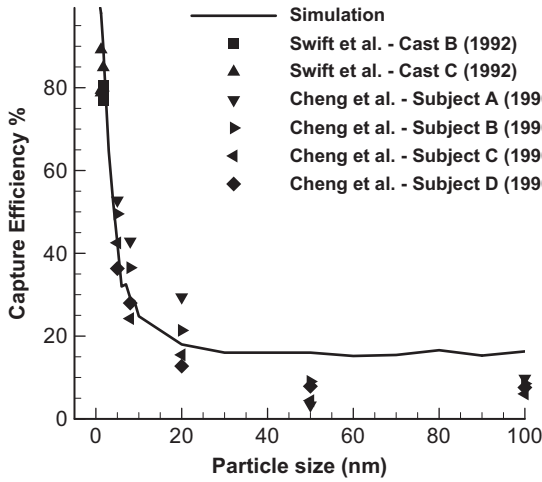$$Pe = \frac{Q}{DL_s}$$

(35)

FIGURE 2.11 Comparison of the simulation results for the nose capture efficiency with the experimental data for particles of different sizes.

where L_s the length of the nasal passage, Q is the flow rate, and D is the particle diffusivity. While there is some slight scatter for large values of Pe, it is seen that the simulation result for a range of parameters collapses to a single curve. That is as expected and, for ultrafine particles, the deposition process is dominated by the diffusion.

An empirical equation given by

$$\eta = 100\left(1 - 0.88e^{-218Pe^{-0.75}}\right) \tag{36}$$

may be fitted to the simulation results in Fig. 12. This figure shows that Eqn (36) provides a good fit to the simulation results. As the Peclet number increases, which is associated with larger particle size, some scatters appear in
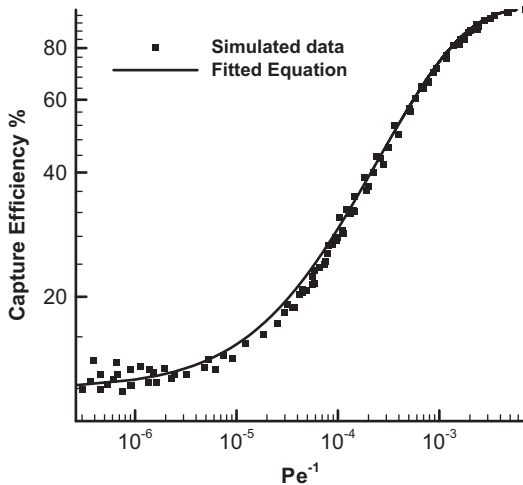

FIGURE 2.12 Variations of nose capture efficiency with inverse Peclet number for particles smaller than 100 nm.
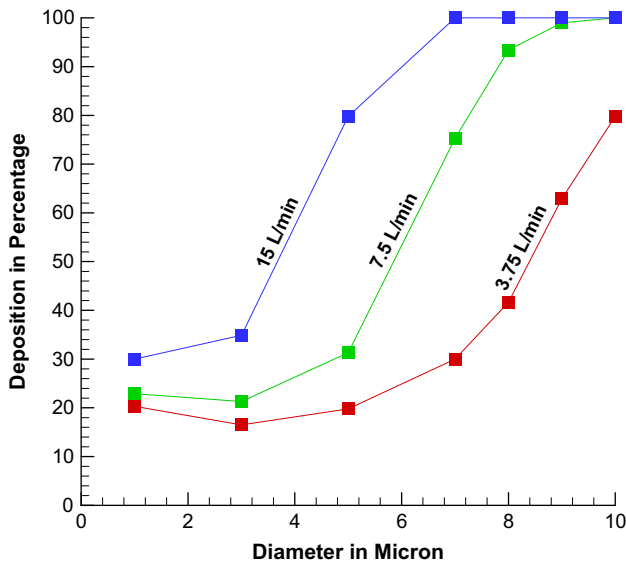
FIGURE 2.13   Simulation results for the nose capture efficiency for particle of different sizes at different breathing rate.

the simulation results. This suggests that for larger particles, in addition to the Peclet number, the capture efficiency could also depend on Stokes number. Zamankhan et al. [93] used a more refined mesh and found slightly different expression for the fit to the simulation results.

For breathing rates of 3.75, 7.5, and 15 L/min, the capture efficiency of the nose for particles in the size range of 200 nm–10 μm was evaluated and results are shown in Fig. 2.13. It is seen that the capture efficiency increases as particle size increases. Furthermore, as the inspiratory flow rate increases, there is a marked increase in the capture efficiency of the nose.

The simulation results presented in Fig. 2.13 are replotted in Fig. 2.14 versus Stokes number. It is seen that the simulation results collapse to a single curve. This observation suggests that inertia impaction is the key mechanism for the deposition of large particles in the nasal passages.

4. CONCLUSIONS

In this chapter, the fundamentals of computational modeling of particles transport and deposition were reviewed and some applications were described. Particular attention was given to transport and deposition processes in lung bifurcations and nose. The presented results showed that:

- The molecular diffusion and turbulence are dominant for deposition of nanometer size particles and the deposition rate increases as particle diameter decreases.
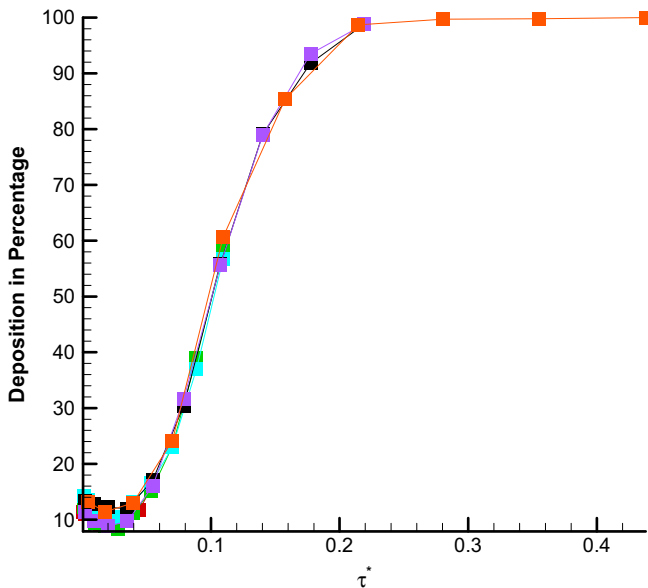
FIGURE 2.14 Variations of nose capture efficiency with Stokes number for particles in the size range of 200 nm–10 μm.

- For particles larger than a few microns, the impaction is the dominant deposition mechanism and the deposition rate increases with the particle size.
- Turbulence in the airflow in the upper airway affects the capture efficiency.
- Computer simulation results are in good agreement with the available experimental data.

ACKNOWLEDGMENTS

REFERENCES

[1] N.A. Fuchs, The Mechanics of Aerosols, Pergamon Press, Oxford, UK, 1964.
[2] S.K. Friedlander, Smoke, Dust and Haze – Fundamentals of Aerosol Behaviour, John Wiley & Sons, New York, NY, 1977.
[3] W.C. Hinds, Aerosol Technology, Properties, Behavior, and Measurement of Airborne Particles, John Wiley & Sons, New York, NY, 1982.
[4] K.L. Mittal (Ed.), Particle on Surfaces: Detection, Adhesion and Removal, vol. 1–3, Plenum Press, New York, NY, 1988, 1989, 1991.

[5] D.J. Quesnel, D.S. Rimai, L.H. Sharpe, Particle Adhesion: Applications and Advances, Taylor and Francis, New York, NY, 2001.

[6] S.K. Friedlander, H.F. Johnstone, Deposition of suspended particles from turbulent gas streams, Ind. Eng. Chem. 49 (1957) 1151.

[7] J. Fernandez de la Mora, S.K. Friedlander, Aerosol and gas deposition to fully rough surfaces: filtration model for blade-shaped elements, Int. J. Heat Mass Transfer 25 (1982) 1725.

[8] J.W. Cleaver, B. Yates, A sublayer model for deposition of particles from turbulent flows, Chem. Eng. Sci. 30 (1975) 983.

[9] M. Fichman, C. Gutfinger, D. Pnueli, A model for turbulent deposition of aerosols, J. Aerosol Sci. 19 (1988) 123.

[10] F.G. Fan, G. Ahmadi, A sublayer model for turbulent deposition of particles in vertical ducts with smooth and rough surfaces, J. Aerosol Sci. 24 (1993) 45.

[11] F.G. Fan, G. Ahmadi, On the sublayer model for turbulent deposition of particles in presence of gravity and electric fields, Aerosol Sci. Technol. 21 (1994) 49.

[12] F.G. Fan, G. Ahmadi, Dispersion of ellipsoidal particles in an isotropic pseudo-turbulent flow field, ASME J. Fluid Eng. 117 (1995) 154.

[13] F.G. Fan, G. Ahmadi, A sublayer model for wall deposition of ellipsoidal particles in turbulent stream, J. Aerosol Sci. 25 (1995) 813.

[14] F.G. Fan, G. Ahmadi, Wall deposition of small ellipsoids from turbulent air flow – a Brownian dynamics simulation, J. Aerosol Sci. 31 (2000) 1205.

[15] A. Li, G. Ahmadi, Dispersion and deposition of spherical particles from point sources in a turbulent channel flow, Aerosol Sci. Technol. 16 (1992) 209.

[16] A. Li, G. Ahmadi, Deposition of aerosol on surfaces in a turbulent channel flow, Int. J. Eng. Sci. 31 (1993) 435.

[17] A. Li, G. Ahmadi, Computer simulation of deposition of aerosols in a turbulent channel flow with rough walls, Aerosol Sci. Technol. 18 (1993) 11.

[18] A. Li, G. Ahmadi, Aerosol particle deposition with electrostatic attraction in a turbulent channel flow, J. Colloid Interf. Sci. 158 (1993) 476.

[19] C. He, G. Ahmadi, Particle deposition in a nearly developed turbulent duct flow with electrophoresis, J. Aerosol Sci. 30 (1999) 739.

[20] M. Shams, G. Ahmadi, H. Rahimzadeh, A sublayer model for deposition of nano- and microparticles in turbulent flows, Chem. Eng. Sci. 55 (2000) 6097.

[21] A. Li, G. Ahmadi, R. Bayer, M.A. Gaynes, Aerosol particle deposition in an obstructed turbulent duct flow, J. Aerosol Sci. 25 (1994) 91.

[22] G. Ahmadi, D.H. Smith, Particle transport and deposition in a hot-gas cleanup pilot plant, Aerosol Sci. Technol. 29 (1998) 183.

[23] J.B. McLaughlin, Aerosol particle deposition in numerically simulated channel flow, Phys. Fluids A 7 (1989) 1211.

[24] H. Ounis, G. Ahmadi, J.B. McLaughlin, Dispersion and deposition of Brownian pericles from point sources in a simulated turbulent channel flow, J. Colloid Interf. Sci. 147 (1991) 233.

[25] H. Ounis, G. Ahmadi, J.B. McLaughlin, Brownian Particle deposition in a directly simulated turbulent channel flow, Phys. Fluids A 5 (1993) 1427.

[26] K.D. Squires, J.K. Eaton, Preferential concentration of solid particles by turbulence, Phys. Fluids A 3 (1991) 1169.

[27] M. Soltani, G. Ahmadi, Direct numerical simulation of particle entrainment in turbulent channel flow, Phys. Fluids A 7 (1995) 647.

[28] M. Soltani, G. Ahmadi, Direct numerical simulation of curly fibers in turbulent channel flow, Aerosol Sci. Technol. 33 (2000) 392.

[29] M. Soltani, G. Ahmadi, H. Ounis, J.B. McLaughlin, Direct numerical simulation of charged particle deposition in a turbulent channel flow, Int. J. Multiphase Flow 24 (1998) 77.

[30] H. Zhang, G. Ahmadi, Aerosol particle transport and deposition in vertical and horizontal turbulent duct flows, J. Fluid Mech. 406 (2000) 55.

[31] Q. Wang, K.D. Squires, M. Chen, J.B. McLaughlin, On the role of the lift force in turbulence simulations of particle deposition, Int. J. Multiphase Flow 23 (1994) 749.

[32] J.B. McLaughlin, Numerical computation of particles–turbulence interaction, Int. J. Multiphase Flow 20 (1994) 211.

[33] D.W. Cooper, M.H. Peters, R.J. Miller, Predicted deposition of submicrometer particles due to diffusion and electrostatics in viscous axisymmetric stagnation-point flow, Aerosol Sci. Technol. 11 (1989) 133.

[34] D.W. Cooper, R.J. Miller, J.J. Wu, M.H. Peters, Deposition of submicron aerosol particles during integrated circuit manufacturing: theory, Part. Sci. Technol. 8 (1990) 209.

[35] D.J. Rader, A.S. Geller, Transport and Deposition of Aerosol Particles, in: R. Kohli, K.L. Mittal (Eds.), Developments in Surface Contamination and Cleaning. Fundamentals and Applied Aspects, William Andrew Publishing, Norwich, NY, 2008, pp. 189–266.

[36] C.-H. Lin, C. Zhu, Relevance of particle transport in surface deposition and cleaning, in: R. Kohli, K.L. Mittal (Eds.), Developments in Surface Contamination and Cleaning. Fundamentals and Applied Aspects, William Andrew Publishing, Norwich, NY, 2008, pp. 267–297.

[37] D.-L. Liu, Particle Deposition onto Enclosure Surfaces, in: R. Kohli, K.L. Mittal (Eds.), Developments in Surface Contamination and Cleaning. Particle Deposition, Control and Removal, vol. 2, Elsevier, Oxford, UK., 2010, pp. 1–56.

[38] F. White, Viscous Flow, McGraw Hill, New York, NY, 1974.

[39] H. Schlichting, Boundary Layer Theory, McGraw Hill, New York, NY, 1979.

[40] J.O. Hinze, Turbulence, McGraw Hill, New York, NY, 1975.

[41] B.E. Launder, D.B. Spalding, Mathematical Models of Turbulence, Academic Press, New York, NY, 1972.

[42] W.P. Jones, B.E. Launder, The calculation of low Reynolds number phenomena with a two-equation model of turbulence, Int. J. Heat Mass Transfer 16 (1973) 1119.

[43] B.E. Launder, G.J. Reece, W. Rodi, Progress in development of a Reynolds-stress turbulence closure, J. Fluid Mech. 68 (1975) 537.

[44] W. Kvasnak, G. Ahmadi, D.J. Schmidt, An engineering model for the fuel spray formation of deforming droplets, Atomization and Sprays 14 (2004) 289.

[45] D.J. Thomson, Criteria for the selection of stochastic models of particle trajectories in turbulent flows, J. Fluid Mech. 180 (1987) 529.

[46] L. Tian, G. Ahmadi, Particle deposition in turbulent duct flows – comparisons of different model predictions, J. Aerosol Sci. 38 (2007) 377.

[47] N.B. Wood, A simple method for calculation of turbulent deposition to smooth and rough surfaces, J. Aerosol Sci. 12 (1981) 275.

[48] N.B. Wood, The mass transfer of particles and acid vapour to cooled surfaces, J. Inst. of Energy 76 (1981) 76.

[49] P.G. Papavergos, A.B. Hedley, Particle deposition behavior from turbulent flow, Chem. Eng. Res. Des. 62 (1984) 275.

[50] M. Soltani, G. Ahmadi, Charged particle trajectory statistics and deposition in a turbulent channel flow, Aerosol Sci. Technol. 31 (1999) 170.

[51] T.L. Chan, R.M. Schreck, Effect of the laryngeal jet in the human trachea and upper bronchial airways, J. Aerosol Sci. 11 (1980) 447.

[52] J. Heyder, J. Gebhart, G. Rudof, C.F. Schiller, W. Stahlhofen, Deposition of particles in the human respiratory tract in the size range 0.005–15 μm, J. Aerosol Sci. 17 (1986) 811.

[53] J.R. Johnson, R.C. Schroter, Deposition of particles in model airways, J. Appl. Physiol 47 (1979) 947.

[54] C.S. Kim, A.J. Iglesias, Deposition of inhaled particles in bifurcating airways models: i. Inspiratory deposition, J. Aerosol Med. 2 (1989) 1.

[55] C.S. Kim, D.M. Fisher, D.J. Lutz, T.R. Gerrity, Particle deposition in bifurcating airway models with varying airway geometry, J. Aerosol Science 25 (1994) 567.

[56] C.S. Kim, D.M. Fisher, Deposition of aerosol particles in successively bifurcating airways models, Aerosol Sci. Technol. 31 (1999) 198.

[57] B.S. Cohen, R.G. Sussman, M. Lippmann, Ultrafine particle deposition in a human tracheobronchial cast, Aerosol Sci. Technol. 12 (1990) 1082.

[58] D.L. Swift, N. Montassier, P.K. Hopke, K. Karpen-Hayes, Y.S. Cheng, Y.F. Su, H.C. Yeh, J.C. Strong, Inspiratory deposition of ultrafine particles in human nasal replicate casts, J. Aerosol Sci. 23 (1992) 65.

[59] B.S. Cohen, B. Asgharian, Deposition of ultrafine particles in the upper airways: an empirical analysis, J. Aerosol Sci. 21 (1990) 789.

[60] B. Asgharian, O.T. Price, W. Hofmann, Prediction of particle deposition in the human lung using realistic models of lung ventilation, J. Aerosol Sci. 37 (2006) 1209.

[61] T.B. Martonen, Y. Yang, R.C. Lessmann, Fluid Dynamics of the human larynx and upper tracheobronchial airways, Aerosol Sci. Technol. 19 (1993) 133.

[62] T.B. Martonen, Y. Yang, Z.Q. Xue, Effects of carinal ridge shapes on lung airstreams, Aerosol Sci. Technol. 21 (1994) 119.

[63] I. Balashazy, W. Hofmann, Particle deposition in airway bifurcations: I-inspiratory flow, J. Aerosol Science vol. 24 (1993) 745–772.

[64] I. Balashazy, W. Hofmann, Particle deposition in airway bifurcations: II-expiratory flow, J. Aerosol Science vol. 24 (1993) 773–786.

[65] I. Balashazy, Simulation of particle trajectories in bifurcating tubes, J. Comput. Phys. 110 (1994) 80.

[66] B. Asgharian, S. Anjilvel, Inertial and gravitational deposition of particles in a square cross section bifurcating airway, Aerosol Sci. Technol. 20 (1994) 177.

[67] A. Li, G. Ahmadi, Computer simulation of particle deposition in the upper tracheobronchial tree, Aerosol Sci. Technol. 23 (1995) 201.

[68] I. Balashazy, W. Hofmann, T. Heistracher, Computation of local enhancement factors for the quantification of particle deposition patterns in airway bifurcations, J. Aerosol Sci. 30 (1999) 185.

[69] J.K. Comer, C. Kleinstreuer, S. Hyun, C.S. Kim, Aerosol transport and deposition in sequentially bifurcation airways, ASME J. Biomech. Eng. 122 (2000) 152.

[70] Z. Zhang, C. Kleinstreuer, C.S. Kim, Flow structure and particle transport in a triple bifurcation airway model, J. Fluids Eng. 123 (2001) 320.

[71] Z. Zhang, C. Kleinstreuer, J.F. Donohue, C.S. Kim, Comparison of micro- and nano-size particle depositions in a human upper airway model, J. Aerosol Sci. 36 (2005) 211.

[72] Z. Zhang, C. Kleinstreuer, Modeling of low Reynolds number turbulent flows in locally constricted conduits: a comparison study, AIAA Journal 41 (2002) 831.

[73] Z. Zhang, C. Kleinstreuer, Airflow structures and nano-particle deposition in a human upper airway model, J. Comput. Phys. 198 (2004) 178.

[74] L. Tian, G. Ahmadi, P.K. Hopke, (July 2006). Flow and particle deposition in asymmetric human airways. Paper FEDSM2006–98198, ASME 2nd Joint U.S. – European Fluids Engineering Summer Meeting. doi:10.1115/FEDSM2006-98198.

[75] E.R. Weibel, Morphometry of the Human Lung, Academic Press, New York, NY, 1963.

[76] O.G. Raabe, H.C. Yeh, G.M. Schum, R.F. Phalen, Tracheobronchial Geometry: Human, Dog, Rat and Hamster. Report LF53, Lovelace Foundation for Medical Education and Research, Albuquerque, NM, 1976.

[77] D.L. Swift, D.F. Proctor, Access of air to the respiratory tract, in: J.D. Brian, D.F. Proctor, L.M. Reid (Eds.), Respiratory Defense Mechanisms: Part 1, Marcel Dekker, New York, NY, 1977, pp. 63–93.

[78] S. Schreck, K.J. Sullivan, C.M. Ho, H.K. Chang, Correlations between flow resistance and geometry in a model of the human nose, J. Appl. Physiol. 75 (1993) 1767.

[79] I. Hahn, P.W. Scherer, M.M. Mozell, Velocity profiles measured for airflow through a large-scale model of the human nasal cavity, J. Appl. Physiol. 75 (1993) 2273.

[80] J.T. Kelly, A.K. Prasad, A.S. Wexler, Detailed flow patterns in the nasal cavity, J. Appl. Physiol. 89 (2000) 323.

[81] K. Keyhani, P.W. Scherer, M.M. Mozell, Numerical simulation of airflow in the human nasal cavity, J. Biomech. Eng. 117 (1995) 429.

[82] R.P. Subramanian, R.B. Richardson, K.T. Morgan, J.S. Kimbell, R.A. Guilmette, Computational fluid dynamics simulations of inspiratory airflow in the human nose and nasopharynx, Inhal. Toxicol. 10 (1998) 91.

[83] Y.S. Cheng, Y. Yamada, H.C. Yeh, D.L. Swift, Diffusional deposition of ultrafine aerosols in a human nasal cast, J. Aerosol Sci. 19 (1988) 741.

[84] Y.S. Cheng, Y.F. Su, H.C. Yeh, D.L. Swift, Deposition of thoron progeny in human head airways, Aerosol Sci. Technol. 18 (1993) 359.

[85] D.L. Swift, J.C. Strong, Nasal deposition of ultrafine 218Po aerosols in human subjects, J. Aerosol Sci. 27 (1996) 1125.

[86] J.C. Strong, D.L. Swift, Deposition of ultrafine particles in a human nasal cast, in: Proceedings of the 1st Conference of Aerosol Society, Loughborough University of Technology, Leicestershire, UK., 1987, pp. 109–112.

[87] Y.S. Cheng, Y. Zhou, B.T. Chen, Particle deposition in a cast of human oral airways, Aerosol Sci. Technol. 31 (1999) 286.

[88] Y.S. Cheng, Aerosol deposition in the extrathoracic region, Aerosol Sci. Technol. 37 (2003) 659.

[89] T.B. Martonen, Z. Zhang, G. Yu, C.J. Musante, Fine particle deposition within human nasal airways, Inhal. Toxicol. 15 (2003) 283.

[90] J.T. Kelly, B. Asgharian, J.S. Kimbell, B.A. Wong, Particle deposition in human nasal airway replicas manufactured by different methods. Part II: ultrafine particles, Aerosol Sci. Technol. 38 (2004) 1072.

[91] G. Yu, Z. Zhang, R. Lessmann, Fluid flow and particle diffusion in the human upper respiratory system, Aerosol Sci. Technol. 2 (1998) 146.

[92] P.W. Scherer, K. Keyhani, M.M. Mozell, Nasal dosimetry modeling for humans, Inhal. Toxicol. 6 (1994) 85.

[93] P. Zamankhan, G. Ahmadi, Z. Wang, P.K. Hopke, W.-C. Su, Y.-S. Cheng, D. Leonard, Airflow and deposition of nano-particles in human nasal cavity, Aerosol Sci. Technol. 40 (2006) 463.

[94] K.T. Shanley, P. Zamankhan, G. Ahmadi, P.K. Hopke, Y-S. Cheng, Numerical simulations investigating the regional and overall deposition efficiency of the human nasal cavity, J. Inhal. Toxicol. 20 (2008) 1093.

[95] S. Y-Cheng, H.C. Yeh, R.A. Guilmette, S.Q. Simpson, K.H. Cheng, D.L. Swift, Nasal deposition of ultrafine particles in human volunteers and its relationship to airway geometry, Aerosol Sci. Technol. 25 (1996) 274–291.